JOURNAL OF MATERIALS SCIENCE 32 (1997) 2735–2744

Simplified elastic models for disk-shaped precipitates

C. R. HOUSKA
Department of Materials Science and Engineering, Virginia Polytechnic Institute and State University, Blacksburg, VA 24061 USA

RADOMÍR KUŽEL
Department of Semi-Conductor Physics, Charles University, Praha 2, Czech Republic

A procedure is presented to calculate the elastic displacement fields found in the early stages of coherent precipitation in age hardenable alloys. The procedure is designed for a subsequent calculation of X-ray diffraction profiles. Displacement fields from precipitates of finite size having local order may be examined with reduced computer times. Point sources consisting of a doublet combined with a spherical field are distributed over the plane of a disk shaped precipitate. The relative strength of this combination is adjustable; however, the total strength is scaled to be in agreement with lattice parameter data. An empirical correction for elastic anisotropy, is guided by Green's function calculations. Examples are given for calculating fields from single disks and stair step pairs. These calculations may be carried out with reduced computer time. This is made possible by reducing a large number of uniformly distributed point sources to an optimum number having weighted strengths and special locations throughout the plane of a disk. In order to assess directional effects and more readily relate the displacements to diffraction data, projected displacements are used. The tetragonality of the interplanar *d*-spacings is examined within zones of severe deformation located in the immediate vicinity of the precipitate.

1. Introduction

Analytical procedures are available to calculate the anisotropic elastic displacement fields created by disk [1] and ellipsoidal precipitates [2] that show misfit with the surrounding matrix. Although these Green function calculations provide useful and accurate files of the displacements from single precipitates, they are less convenient when interacting arrays of precipitates are examined because of the considerable computer time involved. The difficulties become even greater when these numerical files serve as input for other calculations that model experimental data. There is a need for a simple analytical formulation for displacement fields, with a minimum number of parameters, that requires an order of magnitude less computer time so that arrays of precipitates can be examined and compared with experimental data.

Two related asymptotic models developed by Keating and Goland (K–G) are of special interest. The first [3] deals with a field having tetragonal symmetry about an interstitial atom in an isotropic lattice. As an isotropic calculation, the field typically differs from more exact anisotropic Green function calculations. A simple trigonometric function is introduced to reshape the field so that it appears like the more exact anisotropic calculations for a range of elastic constants. This tetragonal field requires a combination of pure doublet and point sources. The doublet and spherical strength parameters are allowed to vary to fit the conditions of the specific problem. Lattice parameter data are used to determine the overall strength of the field [4]. In a second calculation, treating prismatic loops in an isotropic medium, Keating and Goland [5] calculated the elastic displacement field produced by the insertion of an incompressible disk in a circular incision or the removal of a like amount of material. This was initially developed to represent a continuum calculation of the elastic field from an interstitial or vacancy loop. A displacement of $\pm b/2$ was imposed perpendicular to the plane of the loop within its circumference and zero outside. At large distances from the loop, the exact expression for the field converges to that of a point source with spherical symmetry and a single doublet oriented perpendicular to the loop plane. This combination introduces lattice displacements with tetragonal symmetry. The strengths of the two singularities depend upon "*b*", the loop area and Poisson's ratio. Like the interstitial, the combination of a doublet without moment and spherical field imparts tetragonal symmetry to the displacement field. However, in this case, the imposed boundary conditions applied to the inclusion gives inter-related spherical and doublet strengths. This restriction is eliminated in our development in order to

0022–2461 © *1997 Chapman & Hall*

deal with observable transformation strains relating to precipitation problems.

Our model for a disk-shaped precipitate, is developed from the asymptotic field for the interstitial but is modified to include an empirical term for elastic anisotropy. The field for a disk is obtained by summing over a uniform distribution of centres in the plane of the disk and contains an adjustable parameter which allows for a range of transformation strains. Symmetry is assumed about the disk axis.

The interacting fields from two disks in an array is obtained by super position. A stair-step configuration along [110] directions is of special interest for aged Cu–Be. This has been considered previously for an isotropic matrix [6, 7]. In a parallel paper, the authors, introduced this field into diffraction calculations to quantitatively model the Bragg and diffuse scattering from the distorted matrix. A stair-step model is believed to be particularly important when this alloy is aged at low temperatures.

2. Displacement fields

2.1. Point field-anisotropy

Undersize or oversize atoms within a disk-shaped precipitate are assumed to contribute individually as a sum of doublet and spherical disturbances. The isotropic formulation by K–G [3] is given by

$$\vec{\mu}(r, \phi) = \frac{\vec{A}_{KG}}{r^2}, \tag{1}$$

with

$$\vec{A}_{KG} = \vec{i}_r \left\{ C_d \left[-\frac{\lambda + \mu}{2\mu} + \frac{5\mu + 3\lambda}{2\mu} \cos^2 \phi \right] + C_s \right\} - \vec{i}_\phi C_d \sin \phi \cos \phi \tag{2}$$

where $\vec{A}_{KG}$ is the vector strength given in terms of unit vectors along r and ϕ in the spherical coordinate system, C_d is the doublet strength, and C_s the strength of the spherical disturbance. The strength terms have been related to the volume size factor, V_{SF}, atomic volume, V_a, and the Eshelby factor γ [8].

$$\gamma = 3 \frac{\lambda + 2\mu}{3\lambda + 2\mu} \tag{3}$$

with Lame constants

$$\lambda = \tfrac{1}{5}(C_{11} + 4C_{12} - 2C_{44}) \tag{4}$$

$$\mu = \tfrac{1}{5}(C_{11} - C_{12} + C_{44}) \tag{5}$$

expressed in terms of single crystal elastic constants.

and

$$C_s = (1 - C_{sd}) \frac{V_{SF} V_a}{4\pi\gamma}, \; C_d = 3C_{sd} \frac{V_{SF} V_a}{4\pi\gamma} \tag{6}$$

$$C_{sd} = \frac{C_d}{3C_s + C_d} = \frac{P_{33} - P_{11}}{2P_{11} + P_{33}} \tag{7}$$

with P_{33} and $P_{11} = P_{22}$ representing the components of the dipole tensor for a tetragonal field [9]. Integrating Equation 1 over a spherical surface surrounding the point defect gives a volume change $V_{SF} V_a/\gamma$ per defect in an infinite medium. The terms V_{SF} and V_a are conveniently tabulated by King [4] and refer to measurable volume changes in crystals of finite size.

The effect of elastic anisotropy may be examined by making a comparison with Green function field calculations. This has been done for a range of interstitial systems using the original K–G function in references [10, 11]. Differences are found between isotropic and anisotropic calculations except for the case of tungsten which is elastically isotropic. The departures are most evident at $\phi \approx 0^\circ$ and 30°, and have planar symmetry with respect to the z-axis. A small variation in the field occurs about the z-axis in the Green function calculations, this is neglected and rotational symmetry is assumed. Wing-shaped displacement contours become increasingly apparent as the anisotropy factor

$$C_e = 1 - \frac{C_{11} - C_{12}}{2C_{44}} \tag{8}$$

becomes more positive, while a negative C_e extends the iso-displacement contours along the z-axis. Introducing an additive empirical correction of the form

$$f(C_e) \cos 4\phi \cos^2 \phi \tag{9}$$

with

$$f(C_e) = 0.15 \text{ erf } C_e \tag{10}$$

produces wing-shaped contours close to 30° for $f(C_e > 0)$ and if $f(C_e < 0)$ the field becomes extended along z as it does for the more exact calculations. The following approximates the field from Green function calculations

$$\vec{\mu}(r, \phi, C_{sd}, C_e) = \frac{\vec{A}(\phi, C_{sd}, C_e)}{r^2}, \tag{11}$$

with

$$\vec{A}(\phi, C_{sd}, C_e) = \frac{V_{SF} V_a}{4\pi\gamma} \left\{ \frac{\vec{i}_r}{2} (C_{sd} E_1 [3(1 - f(C_e)) \cos^2 \phi - 8.08 f(C_e) \cos 4\phi \cos^2 \phi - 1] + 2) - \vec{i}_\phi 3 C_{sd} \sin\phi \cos \phi \right\} \tag{12}$$

and

$$E_1 = \frac{5\mu + 3\lambda}{\mu}, \tag{13}$$

Constants are selected in Equation 11 such that the volume change about a single defect remains unchanged at $V_{SF} V_a/\gamma$. Ta and Nb are selected as extreme cases with $C_e = 0.359$ and -0.96 respectively. The shapes of the iso displacement contours shown in Fig. 1(a and b) compare favourably with our previous results [10] and with Figs 5 and 7 of reference [11]. The latter calculations were more strongly based on experimental results. Equation 11, with tetragonal symmetry, will be introduced in a later section for disk calculations.

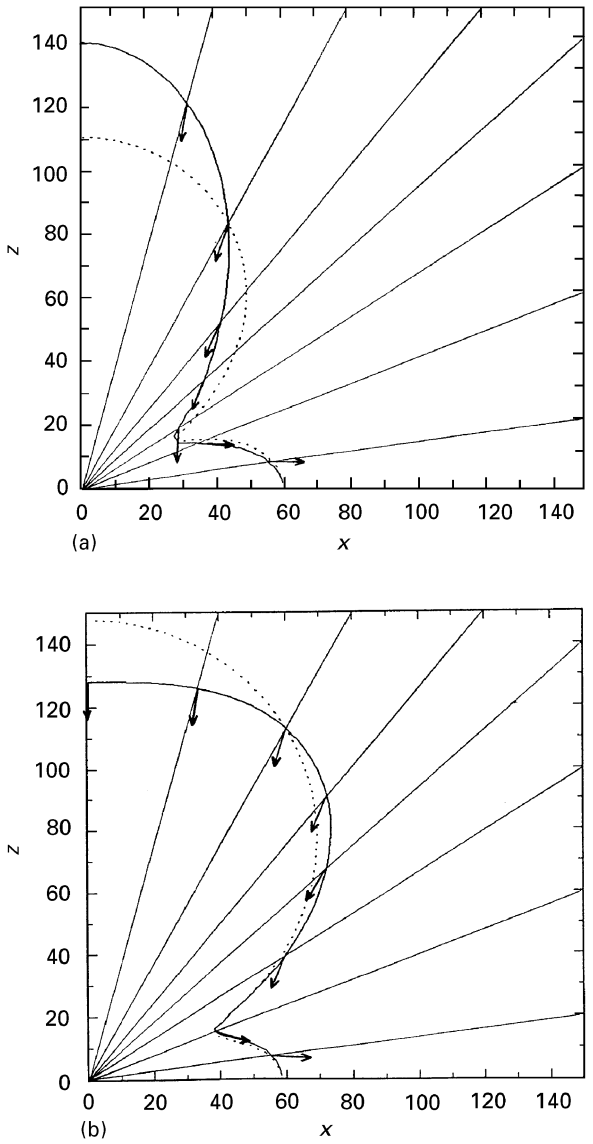

Figure 1 (a) Iso-displacement magnitude contours for point defect (N) in niobium (dots . . . elastically isotropic approximation, solid line . . . elastically anisotropic case calculated with $C_{11} = 240.2$, $C_{12} = 125.6$, $C_{44} = 28.2$ GPa. Other factors used for calculation: $V_{SF} = -0.203$, $V_a = 21.2 \times 10^{-3}$ nm, $C_{SD} = 0.39$. The displacement directions are shown by arrows at selected points. The contour is shown for a displacement of 1.5×10^{-14} m, and (b) Iso-displacement magnitude contours for point defect (N) in tantalum (dots . . . elastically isotropic approximation, solid line . . . elastically anisotropic case calculated with $C_{11} = 260.2$, $C_{12} = 154.5$, $C_{44} = 82.5$ GPa. Other factors used for calculation: $V_{SF} = -0.16$, $V_a = 22.7 \times 10^{-3}$ nm, $C_{SD} = 0.304$. The displacement directions are shown by arrows at selected points. The contour is shown for the displacement of 0.57×10^{-14} m.

2.2. Geometrical considerations

For diffraction calculations, the displacements must be projected onto directions perpendicular to the diffracting planes and summed over all defects for each lattice site. Projection enables one to examine the importance of crystal direction as it relates to static displacements. Fig. 2 illustrates the various angles, shown in stereographic projection, that must be considered. The tetragonal axis normal to the disk is located along the z-axis. Point C locates the normal to the planes (hkl), which is confined to the xz plane,

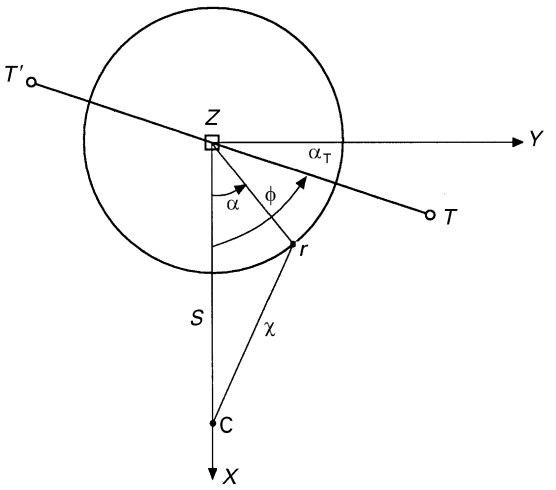

Figure 2 The angles considered in the calculation of the displacement field shown in stereographic projection. S . . . angle between the z-axis and the normal to the planes (hkl), α, ϕ . . . angles defining relative orientation of the point of interest r, χ . . . angle between the normal to the planes (hkl) and the vector r. $T - T'$ define the direction of the stair step.

r locates the angular position for a vector extending from the disk centre to a point in the matrix, and point T gives the relative orientation of a centre line for the stair-step pairing of disks. Angular inter-relationships are visualized in terms of stereographic projections of unit vectors. The angles s, χ, and ϕ form a spherical triangle having sides that are great circles on the surface of a sphere, and α is the angle between planes with sides s and ϕ. The radial projection of r onto a column C is obtained from the spherical triangle i.e., radial distance is multiplied by

$$\cos\chi_r = \cos s \cos\phi + \sin s \sin\phi \cos\alpha \qquad (14)$$

The projection of the tangential component along i_ϕ, which differs by $\frac{\pi}{2}$ from the radial direction, is multiplied by

$$\cos\chi_t = \cos s \cos\left(\phi + \frac{\pi}{2}\right) + \sin s \sin\left(\phi + \frac{\pi}{2}\right)\cos\alpha \qquad (15)$$

Fig. 3(a and b) illustrates a point source located in a disk at an angle, α_d, with radius, r_d. All sources are confined to a planar region $\leqslant r_0$. The matrix point M may be reached from the point source at "i" by the vector, r_i, or from the centre of the disk by r, which make angles, ϕ_i, and ϕ respectively with the z-axis. The corresponding angles with x in the plane x–y are α_d and 0. Both the point field and the point distribution maintain symmetry about the z-axis and give a disk field independent of α.

The disk locations for a two-step source in cartesian coordinates are described by taking disk centres that are spaced by a distance "$2a$" at positions $\pm aC_x$, $\pm aC_y$, $\pm aC_z$, with C_x, C_y, and C_z designating direction cosines for the line connecting disk centres (Fig. 4). The orientation of this line of separation is shown in Fig. 2 by the projected points T and T'. The fields from disks 1 and 2 depend upon the vectors r_1

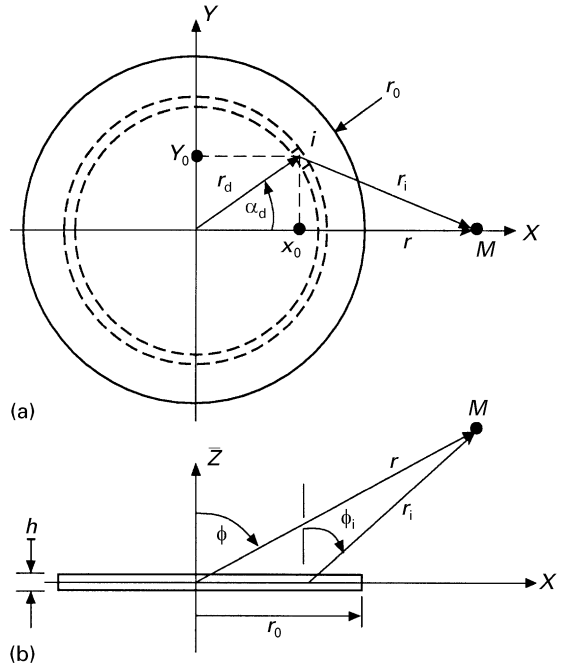

Figure 3 Angles, vectors, and dimensions shown entering calculations for the displacement at the point M caused by point sources i in a disk. (a) Top view and (b) Side view.

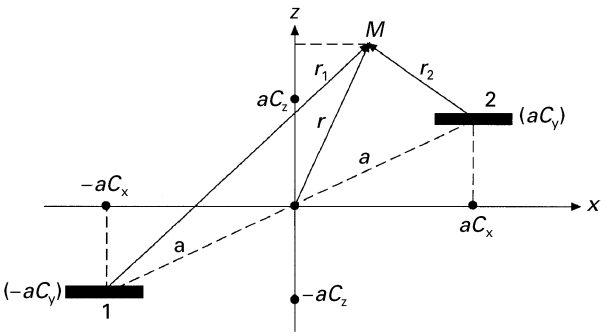

Figure 4 Angles, vectors, and dimensions shown entering calculations for the displacement caused by the pair of disks separated by $2a$.

and r_2 with origins at the disk centres, as well as, the angles ϕ_1 and ϕ_2 which these vectors make with the z-axis. Radial distances and angles for both r_1 and r_2 are written in terms of the single vector r, which is determined by angles ϕ and α, the radial distance, and parameters defining the location of the disks. Expressions for r_1 and r_2, are given in the next section. Rotational symmetry about the z-axis, perpendicular to the disks, is lost in the two-step source unless T and z are parallel i.e., point T coincides with z in the stereographic projection of Fig. 2.

The last geometrical consideration deals with the relative projected displacement of points along a line or along columns "C". Introducing the displacement field with a gradient alters the average interplanar separation, d_0, that exists without the field. Of particular interest for diffraction calculations is the average interplanar spacing within severely distorted zones either in the immediate vicinity of a disk-shaped precipitate or a two-step pair of disks.

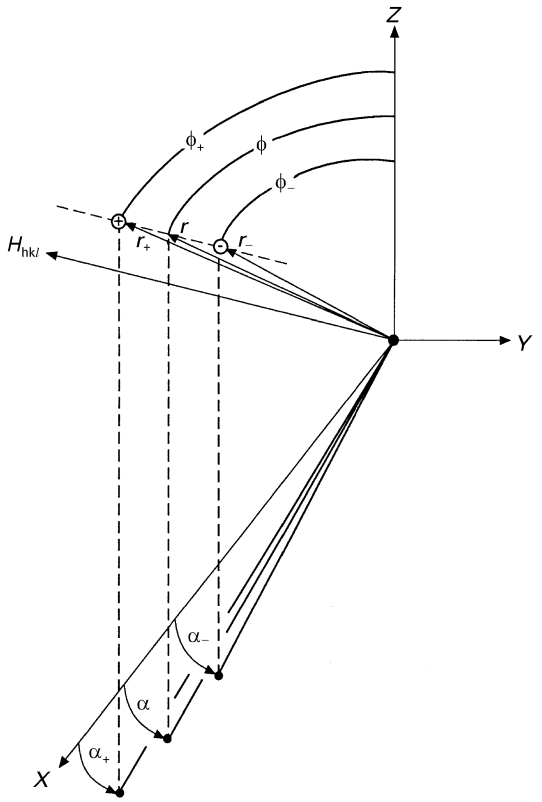

Figure 5 Angles and vectors for describing spacing changes parallel to H_{hkl}.

Fig. 5 illustrates the reciprocal vector H_{hkl} which defines the orientation of the line of projection for columns of cells perpendicular to the reflecting planes (hkl). A line parallel to H_{hkl} extends from points $\oplus$ to $\ominus$. These points are at a distance $\pm\frac{d_0}{2}$ from r with the total distance d_0 representing the spacing of the reflecting planes (hkl). The two points are located from the origin by the vectors r_+ and r_- having spherical angles ϕ_+, α_+, and ϕ_-, α_-. Since H_{hkl} is always taken to be located in the xz plane, the direction cosines for a parallel line extending to points $\oplus$ $\ominus$ is given by C_{XL} and C_{ZL}. A single vector r is used for pair locations along with parameters d_0, C_{XL} and C_{ZL}. The average relative projected spacing change is determined from the appropriate displacement field by summing over all pairs of points with an initial spacing d_0 parallel to H_{hkl}.

2.3. Field calculation for a disk

The total field from all point sources in a disk is expressed in terms of a single radius vector, a set of parameters containing projection angles, and the radius and height of the disk. Individual point sources are projected separately in terms of ϕ_i, and α_i using Equations 14 and 15. These have been defined previously and refer to Fig. 3. Noting that

$$r_d^2 = x_0^2 + y_0^2 \tag{16}$$

with

$$x_0 = r_d \cos\alpha_d,\ y_0 = r_d \sin\alpha_d \tag{17}$$

also

$$r_i^2 = (x - x_0)^2 + (y - y_0)^2 + z^2 \tag{18}$$

or

$$r_i^2 = r^2 + r_d^2 - 2x_0x - 2y_0y \tag{19}$$

and

$$r^2 = x^2 + y^2 + z^2 \tag{20}$$

By using

$$x = r\sin\phi\cos\alpha,\ y = r\sin\phi\sin\alpha,\ z = r\cos\phi \tag{21}$$

and combining terms

$$r_i^2 = r^2\left[1 + \left(\frac{r_d}{r}\right)^2 - 2\left(\frac{r_d}{r}\right)\sin\phi\cos(\alpha - \alpha_d)\right] \tag{22}$$

The angles defining the direction of the infinitesmal source vector, r_i, are

$$\phi_i = \cos^{-1}\left(\frac{z}{r_i}\right) = \cos^{-1}\frac{\cos\phi}{\left[1 + \left(\frac{r_d}{r}\right)^2 - 2\left(\frac{r_d}{r}\right)\sin\phi\cos(\alpha - \alpha_d)\right]^{1/2}} \tag{23}$$

$$\alpha_i = \tan^{-1}\frac{y - y_0}{x - x_0} = \tan^{-1}\left[\frac{\sin\phi\sin\alpha - \left(\frac{r_d}{r}\right)\sin\alpha_d}{\sin\phi\cos\alpha - \left(\frac{r_d}{r}\right)\cos\alpha_d}\right]. \tag{24}$$

While ϕ_i solely influences the strength of source "i", both angles influence the projection onto column "C". If $\mu_i(r, \phi, \alpha, r_d, \alpha_d)$ is the lattice displacement, Equation 11, at r, ϕ, α due to a point source in the disk at r_d, α_d, the total projected displacement onto column, C, due to the full disk for the matrix position r, ϕ, α is obtained by integrating over a uniform distribution of sources within the disk

$$PR\,\mu_d(r, \phi, \alpha) = x_s\frac{h}{V_a}\int_0^{r_0}\int_0^{2\pi} PR\,\mu_i(r, \phi, \alpha, r_d, \alpha_d) \times r_d\,d\alpha_d\,dr_d \tag{25}$$

with

$$PR\,\mu_i(r, \phi, \alpha, r_d, \alpha_d) = \mu_{ri}(r, \phi, \alpha, r_d, \alpha_d)\cos\chi_{ri} + \mu_{ti}(r, \phi, \alpha, r_d, \alpha_d)\cos\chi_{ti} \tag{26}$$

μ_{ri} and μ_{ti} representing the radial and tangential components of Equation 11. V_a is the atomic volume and x_s is the fraction of sites in the precipitate occupied by undersize or oversize solute atoms.

The field calculation for a disk is carried out by numerical integration. In using a Gauss–Legendre Quadrature (GLQ) scheme, the angular and radial integrations over the disk can be expressed as a minimum number of point sources within the confines of the disk. This positions the point sources at special locations with a set of weighting functions that alter the individual strengths of the defects. The total strength remains unaffected by this distribution. We find that the number of sources or the number of points in the quadrature required to describe a displacement largely depends upon the distance from the disk. At large distances, only one point source is required while at the closest distances, the maximum number is required. To a first approximation, the maximum number is determined by the largest spacing of point sources within a disk relative to the distance of the nearest atomic plane in the matrix. The distance to the nearest plane should be greater than the maximum distance between pairs of point sources. This is approximate because the interplay of weighting factors and directional effects from the separate point fields can influence oscillation errors.

For most of the region of interest about a disk, an eight-point quadrature is taken for the integration over α_d and six points over r_d. This gives a total of 48 point sources over the full disk. As the disk is approached closely, additional terms may be required to reduce the oscillations in the numerical results. For this example, the contribution of the projected displacement from each source i is given by the sum

$$PR\,\vec{\mu}_d(r, \phi, \alpha, h, r_0) = \frac{\pi h r_0^2}{4V_a}x_s\sum_{j=1}^{n_r}\sum_{i=1}^{n_{\alpha d}} \times(1 + z_j)w_j w_i PR\,\mu_{ij}\left(r, \phi, \alpha, \tfrac{1}{2}r_0(1 + z_j), \frac{\pi}{2}(1 + z_i)\right) \tag{27}$$

Roots (z_j) and weighting factors are given in reference [12].

The magnitude of the displacement, or vector sum of radial and tangential components, can be plotted in terms of iso displacement contours in a plane passing through the centre of the disk. This is accomplished with Equation 27 by projecting according to Equations 14 and 15 onto a line parallel to r with $\alpha = 0$, and $s = \phi$ for the radial component, and $\alpha = 0$, $s = \phi + \frac{\pi}{2}$ for the tangential.

Fig. 6 illustrates displacement contours and directions for one point defect using Equation 11. The conditions are for the asymptotic field from a single Be atom in a GP zone with $V_{SF} = -0.2645 \times 10^{-3}$ nm^3, $V_a = 11.81 \times 10^{-3}$ nm^3 and $\gamma = 1.32$. A Be atom in the GP zone produces a tetragonal strain with $\varepsilon_{11} = \varepsilon_{22} = 0.112$ and $\varepsilon_{33} = -0.334$. This can be related to C_{sd} according to [13] by;

$$C_{sd} = \frac{(\varepsilon_{33} - \varepsilon_{11})(C_{11} - C_{12})}{(\varepsilon_{33} + 2\varepsilon_{11})(C_{11} + 2C_{12})} \tag{28}$$

where C_{11} and C_{12} are elastic constants. A maximum field strength is found along $\phi \approx 30^\circ$ and a minimum along $\phi \approx 65^\circ$. If GLQ point sources are distributed over a plane for a thin disk of radius 3.5 nm and thickness 0.8 nm (Equation 27), the core region near the disk becomes modified as is shown in Fig. 7. At larger distances, the contours would look like those in

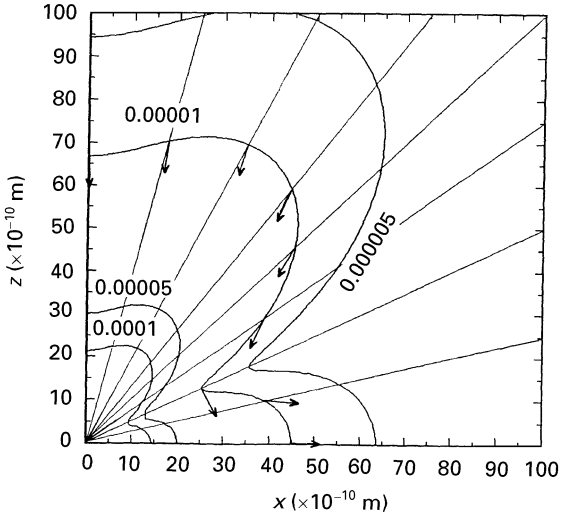

Figure 6 Iso-displacement magnitude contours (in nm) and selected directions for a point defect in copper calculated with the following parameters: $C_{11} = 168.3$, $C_{12} = 121.1$, $C_{44} = 75.7$, $V_{SF} = -0.2645$, $V_a = 11.81 \times 10^{-3}$ nm^3.

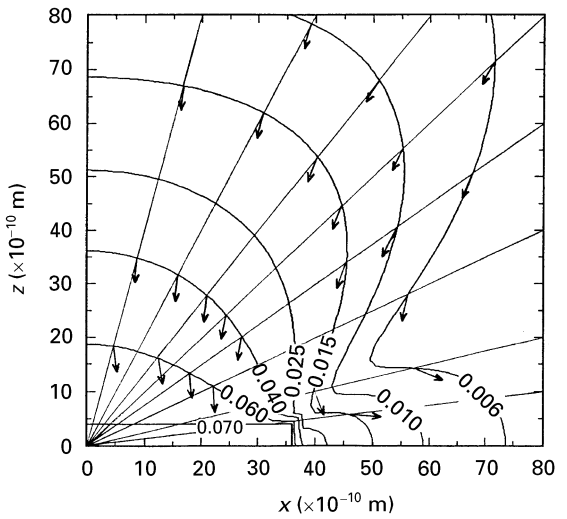

Figure 7 Iso-displacement magnitude contours (in nm) and directions for a disk Cu–50 at % Be in a Cu matrix with a diameter of 7.0 nm and height of 0.8 nm calculated from Equations 25 and 26. Other parameters are the same as for Fig. 6.

Fig. 6 for the asymptotic field. In the core region, the major displacements tend to be perpendicular to the disk while for large distances they are radial. These findings were found to be in agreement with a Green function calculation [13].

Fig. 8(a and b) illustrates the importance of the number of GLQ sources in terms of the z-displacements along the radial directions $\phi = 40^\circ$ (a) and $\phi = 70^\circ$ (b) for a disk with a 3.0 nm radius and 0.29 nm height. The dashed curves were obtained with 48 sources ($n_r = 6$, $n_{\alpha d} = 8$) while the solid was obtained with 600 ($n_r = 15$, $n_{\alpha d} = 40$). The dotted curve is intermediate at 120 sources. Near the surface at $\phi = 0^\circ$, 48 sources are fully adequate, while at $\phi = 40^\circ$ and 70°, oscillations due to the close proximity to individual sources are apparent and a larger number of sources is required. As expected, all three results converge asymptotically as the distance to the point of displacement increases beyond the radius of the disk.

2.4. Stair-step pair

The field from the disk, Equation 27, is used to obtain the field from the stair-step pair of disks whose centres are confined to the line 1–2 (Fig. 4). Each disk is at a distance "a" from the origin and located at ($\pm aC_y$, $\pm aC_y$, $\pm aC_z$). The quantities C_x, C_y and C_z, are direction cosines for the pair. Again, we are interested in determining the projected displacements in the matrix onto columns "C", due to a displacement at position r, ϕ, and α. The field from the two-step pair at disk locations (r_1, ϕ_1, α_1) and (r_2, ϕ_2, α_2) are expressed in terms of "a", and the direction cosines. By using the same procedures as for the disk, one obtains:

$$r_{\frac{1}{2}}^2 = r^2 \left[1 + \left(\frac{a}{r}\right)^2 \pm 2\left(\frac{a}{r}\right)(c_x \sin\phi \cos\alpha + c_y \sin\phi \sin\alpha + c_z \cos\phi) \right] \quad (29)$$

with the $+$ used for r_1 and the $-$ for r_2.

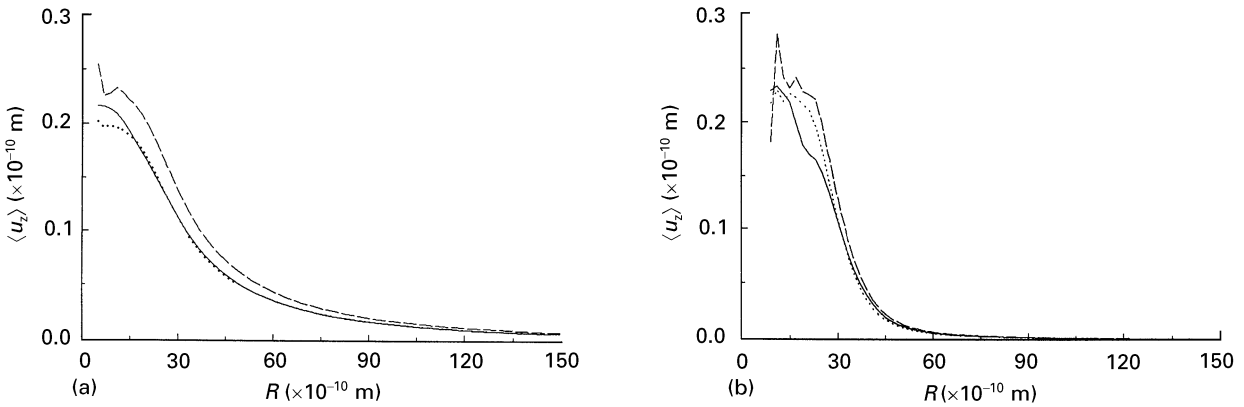

Figure 8 Effect of the number of GLQ sources on the z-displacement along a radial direction at ϕ angles, (a) 40°, (b) 70°. The curves were calculated with the number of GLQ sources along the radial and α directions of (· · ·) 10–12, (– –) 6–8 and (—) 15–40.

Also

$$\phi_{\frac{1}{2}} = \cos^{-1} \frac{\cos\phi \left(\frac{a}{r}\right) c_z}{\left[1 + \left(\frac{a}{r}\right)^2 \pm 2\left(\frac{a}{r}\right)(c_x \sin\phi \cos\alpha + c_y \sin\phi \sin\alpha + c_z \cos\phi)\right]^{1/2}} \tag{30}$$

and

$$\alpha_{\frac{1}{2}} = \tan^{-1}\left[\frac{\sin\phi \sin\alpha}{\sin\phi \cos\alpha \pm \left(\frac{a}{r}\right) c_x}\right] \tag{31}$$

Again, the + and − refer to disks 1 and 2 respectively.

In taking the limit $r \gg a$, the two sources appear as one of double strength when the terms in $(\frac{a}{r})$ vanish. This, of course, provides a major simplification of the field calculations for approximately $r > 20a$.

The projected field for the two-step pair is expressed functionally by:

$$PR\mu_p(r, \phi, \alpha; h, r_0, a, c_x, c_y, c_z) = PR\{\mu_d(r_1, \phi_1, \alpha_1; h, r_0, a, c_x, c_y, c_z) + \mu_d(r_2, d_2, \alpha_2, h, r_0, a, c_x, c_y, c_z))\} \tag{32}$$

with the locations of disks 1 and 2 given in terms of r, ϕ, α from Equations 29–31. Equation 32 represents the sum of projected displacements from all point sources located within both disks. In this example of 6 and 8 point GLQ per disk, a total of 96 terms are taken for both with each term containing a weighted distribution of individual point sources. This, represents a more optimum distribution than one which is uniform in density and weighting factors (references [6, 7].

In order to relate this model with X-ray diffraction (XRD) data, an additional triple integration over r, ϕ and α is required for 2M intensity attenuation factors. This will be presented in a later paper [15]. Lowest order quadratures over a limited region, representing the basic symmetry element within the matrix, must be taken to minimize computer time.

The displacement magnitude contours from a disk with a radius of 3.0 nm and height 0.29 nm are shown in Fig. 9. This can be compared with the displacement fields from a stair-step pairing of disks at an angle of 45° as illustrated in Fig. 10(a–d). The separation between centres is 3.0 nm for (a, b), and 7.0 nm for (c, d). The 45° step introduces an asymmetrically elongated distortion of the contours along the step direction. Displacement contours in the outer region become expanded relative to a single disk (Fig. 9), and new contours of larger displacement magnitudes appear near the outer surfaces (see contours 0.35 to 0.25 in Fig. 10b). This is expected from the addition of fields

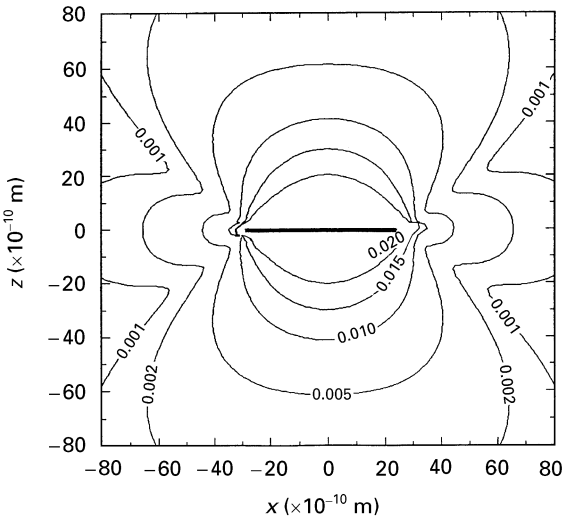

Figure 9 Displacement magnitude contours around a Cu–50 at % Be disk with a 6.0 nm diameter and a unit cell height of 0.29 nm.

in the outside regions. Because of field cancellation in the region between disks, the contours shrink or disappear as their separation decreases. At $a = 3.0$ nm (Fig. 10b), only contours of small displacements are found between disks. However, large displacements are found between edges on each side of a pair which do not cancel. Isodisplacement contours are shown in Fig. 11 (a and b) for the pair of disks with doubled height. There are no important changes in the general shape of the contours rather the values of displacements are increased by a factor of two.

Dimensional changes of the d-spacings along the principal axes are directly relatable to the displacement gradient. This will be considered in the next section.

2.5. Incremental spacing change

In each of the previous calculations, displacements of individual lattice points are of interest. To determine incremental d-spacing changes, pairs of cell displacements are considered along specified directions. The core region about two-step pairs is of special interest. Equation (32) may be used with additional co-ordinate transformations. The radial distances from the origin to undisturbed points separated by d_0 along a column direction is given by

$$r_{\pm}^2 = r^2\left[1 + \left(\frac{d_0}{2r}\right)^2 \pm \left(\frac{d_0}{r}\right)(C_{XL} \sin\phi \cos\alpha + C_{ZL} \cos\phi)\right] \tag{33}$$

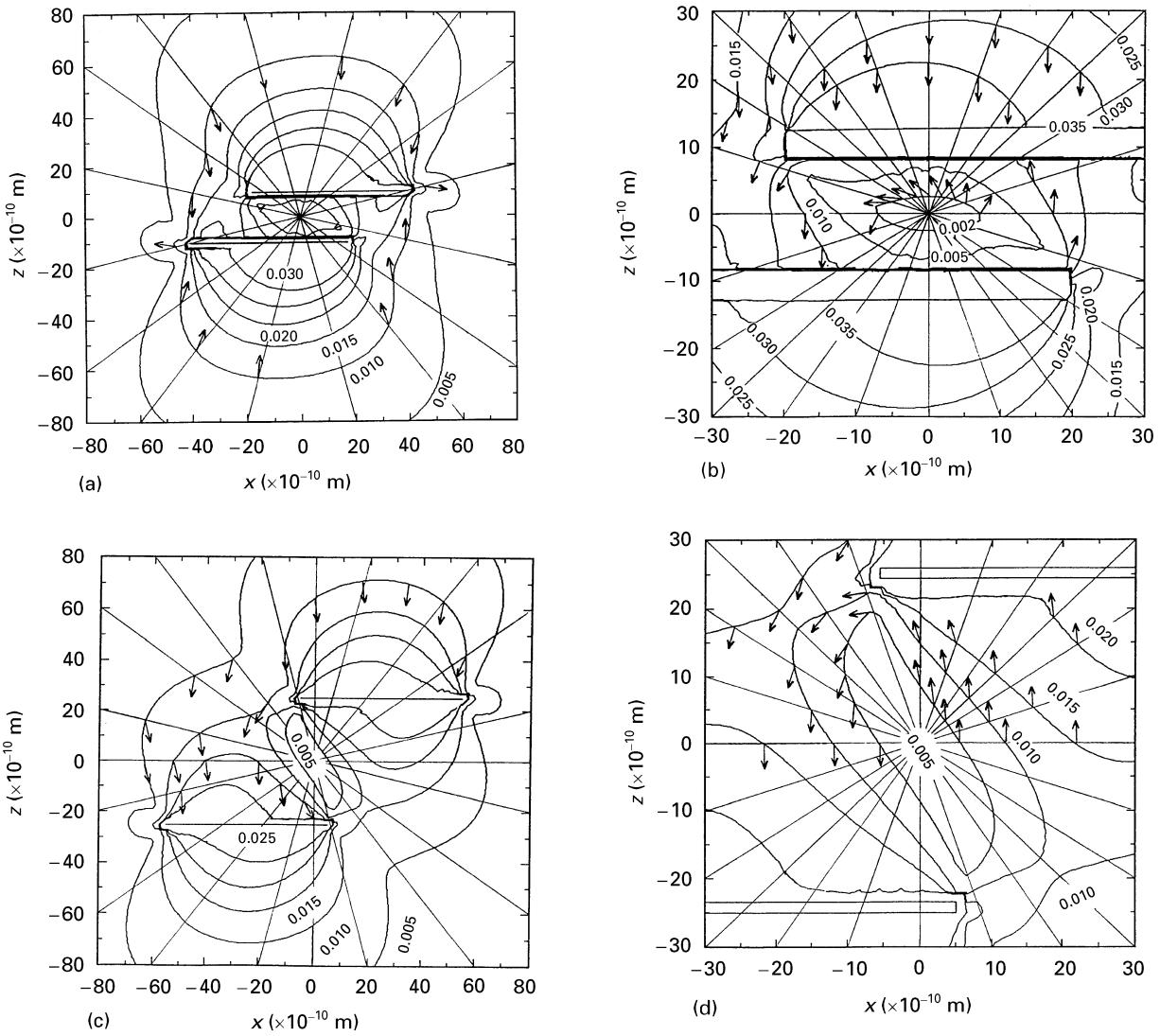

Figure 10 Side view of displacement magnitude contours around a pair of Cu–50 at % Be disks in stair-step (45°). The disks have a common diameter of 6.0 nm and a height of 0.29 nm with centre-to-centre separations of 3.0 nm (a, b), and 7.0 nm (c, d). The displacement directions are shown by arrows at selected points and the corresponding zones between the disks are enlarged in Fig. 10 (b, d).

with angles

$$\phi_{\pm} = \cos^{-1} \times \left\{ \frac{\cos\phi \pm \left(\frac{d_0}{2r}\right) C_{ZL}}{\left[1 + \left(\frac{d_0}{2r}\right)^2 \pm \left(\frac{d_0}{r}\right)(C_{XL}\sin\phi\cos\alpha + C_{ZL}\cos\phi)\right]^{1/2}} \right\} \tag{34}$$

and

$$\alpha_{\pm} = \tan^{-1}\left[\frac{\sin\phi\sin\alpha}{\sin\phi\cos\alpha \pm \left(\frac{d_0}{2r}\right) C_{XL}}\right] \tag{35}$$

For each column direction H_{hkl}, the spacing change expressed in terms of a central vector "r", may be averaged over a range in volume such as the core displacements. This is carried out with the following integral

$$\langle \Delta d \rangle_{hkl} = \frac{\int_{r_0}^{r_k}\int_0^{\pi}\int_0^{\pi} [PR\mu_p(r_+, \phi_+, \alpha_+;\ h, r_0, a, c_x, c_y, c_z) - PR\mu_p(r_-, \phi_-, \alpha_-;\ h,\ r_0, a, c_x, c_y, c_z)] r^2 \sin\phi\, d\alpha\, d\phi\, dr}{\int_{r_0}^{r_k}\int_0^{\pi}\int_0^{\pi} (r^2 \sin\phi\, d\phi\, d\alpha\, dr)} \tag{36}$$

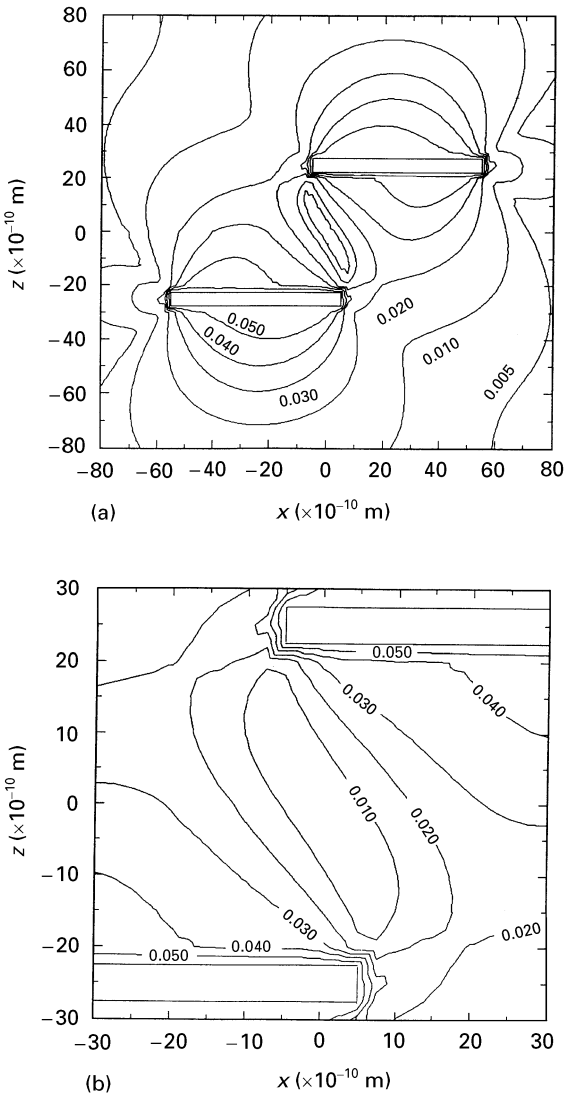

Figure 11 Side view displacement magnitude contours around a pair of Cu–50 at % Be disks with dimensions $2r = 6.0$ nm, $h = 0.58$ nm and separation of 7.0 nm. (a) overall view (b) detailed view between pair.

giving the average change resulting from the field in an infinite medium. The radius vectors r_k and r_0 define a zone of special interest in the matrix starting at the precipitate surface. For example, this might be a zone of severe deformation that extends to r_k which locates a displacement that serves to define a limiting surface. It might also designate a zone of core displacements.

The interplanar spacing in the matrix without defects, d_0, is altered when point defects are introduced. For a finite medium, this is treated in two parts. The first results from the deformation associated with the requirements for a stress-free surface which depends upon (*hkl*) due to the tetragonal nature of the deformation. The second is relatable to the forces associated with the displacement field in an infinite medium. Both are described by K–G in their isotropic description of a tetragonal disturbance from a point source [3]. When both are combined, one arrives at the average *d*-spacing as determined from the Bragg peak of the matrix, d_m, when r_k extends over the entire matrix.

The limits of Equation 36 are defined to exclude the zone within coherent precipitates, which results in spacing changes in the matrix that are opposite to those in the precipitate. For example, a *d*-spacing contraction in the [001] direction within a coherent precipitate produces a field in the matrix that locally expands the *d*-spacings. Likewise an expansion of the precipitate would produce a local contraction of *d*-spacings in the matrix. The diffracted diffuse intensities are displaced accordingly about the Bragg peak. These relative changes have been discussed to describe diffraction effects from *d*-spacing changes about interstitial and vacancy loops [14].

The *d*-spacing changes, calculated from Equation 36, for single disks and for stair-step pairs, are listed for selected directions in Tables I and II respectively. To calculate these averages, a highly deformed matrix zone was defined which extends from the precipitate interface to a surface representing a displacement of 0.015 nm. This displacement surface was located by taking steps along each radial direction so that adjacent points bracket the limiting surface. Each radial distance, r_k, was obtained by interpolation between a pair of adjacent points. A more elaborate procedure had to be used for the field from a pair of disks because the variation with distance does not decrease monotonically. In each case, material within the disks was excluded from the averages.

The results for average *d*-spacing changes should be considered as semiquantitative because Equation 36 normally provides a small difference between numbers that are typically relatively large. Despite this difficulty, the present model does give results that are sufficiently systematic to allow the following conclusions to be made within a highly deformed zone.

(1) The largest increase in average interplanar spacing is along a direction perpendicular to the disk.

TABLE I Average change in interplanar spacing in units of 0.0001 nm for single disks having a height of 0.29 nm with various diameters. S_j locates the angle of inclination relative to the disk plane having a normal along the [001]

Planes	S_j^0	$2r$(nm) 4.0	6.0	9.0
(111)	54.74	3.8	3.1	6.1
(200)	0	10.0	6.6	6.9
–	90	− 0.4	−0.5	0.7

TABLE II Average change in interplanar spacing in units of 0.0001 nm for various interdisk spacings in a 45° stair step. All disks have a diameter of 6.0 nm and a height of 0.29 nm. For the (002) plane, the angle of inclination is 0°, while (a) entries refer to like planes having an angle of inclination of (90°) in the plane containing [001] and a line connecting disk centres. (b) entries refer to a 90° inclination but perpendicular to the plane in (a)

Planes	S_j^0	$2a$(nm) 3.0	5.0	7.0	9.0
(111)	54.74	3.6	4.3	2.3	2.9
	54.74	2.9	4.5	1.0	−1.1
(200)	0	12.5	10.0	8.0	3.7
	(a) 90	2.6	−0.12	−0.65	1.7
	(b) 90	−1.1	−0.06	−0.14	−1.1

It is smaller for ⟨111⟩ directions and often negative in directions parallel to the plane of the disk(s).

(2) Increasing the ratio of disk height to radius, results in greater differences or anisotropy between the average changes for ⟨001⟩ and ⟨111⟩ spacings.

(3) Decreasing the distance between disks in a stair-step increases the anisotropy of interplanar spacings.

Similar calculations carried out for ⟨110⟩ and ⟨311⟩ directions, where other planar angles are examined with respect to the disk planes, are in accord with the preceding conclusions. The ⟨311⟩ set displays an anisotropy similar to the ⟨100⟩ set rather than the ⟨111⟩.

The average mechanical deformations in the Cu-rich matrix about a disk-shape precipitate exhibit a tetragonal symmetry for a single disk in its simplest description. However, this may appear to be monoclinic with stair-step pairs. The average departure from tetragonal symmetry is not large enough to enable a convincing experimental confirmation to be made. This will be discussed further in a subsequent paper dealing with the X-ray diffraction data from a Cu–Be alloy aged at 200 °C [15].

Projected displacements from these simplified models are used to calculate attenuation factors (2M). This includes the projected displacements from all disks over a full range of distances. Tables I and II represent spacing changes in the severely distorted matrix from only primary disks. In a dense system of precipitates with some local order, there are many "secondary" arrangements which are unknown. The overall effect of the resultant secondary field is determined experimentally in terms of an additional distortion of the unit cell obtained from quasiline peak positions.

3. Discussion

When a substitutional atom in the matrix becomes associated with a coherent precipitate, its contribution to the displacement field of the matrix, in general, undergoes a change in symmetry. One example is that of a solute atom in a cubic solid solution that becomes transferred to a flattened ellipsoid or a disk-shaped precipitate that resembles a second equilibrium phase. In this important case, the field in its simplest form changes from one with cubic symmetry to tetragonal symmetry. For a coherent precipitate, the overall strength per defect need not change, but the new symmetry is determined by the transformation strains. This influences the field, as described in this development, through C_{sd} in Equation 28. The development for the displacement fields for finite precipitates and oriented pairs have been based upon the field of a point defect having tetragonal symmetry. This symmetry requires a spherically symmetric point source and a doublet force. The effect of elastic anisotropy is introduced empirically in a way that maintains the simplicity of the K–G analytical result, without changing the overall strength per defect. To generate the field from the precipitate, point sources are distributed uniformly and summed by integration. Numerical integration, using a Gauss–Legendre quadrature effectively reduces the number of point sources to a minimum. The resultant summation contains defects with a nonuniform weighting of strengths and distributed over the plane of a disk. When the field of two or more precipitates are examined, the number of point sources increases linearly with the number in the array and computer time becomes an important consideration. The time consideration becomes even more critical if additional integrations or averaging is required to relate the field to experimental results. Our results for a disk compare well with other more tedious calculations that treat anisotropy directly from first principles.

A stair-step pair of disks show field reinforcement in the exterior region about a pair and cancellation in the volume between the pair. The degree of reinforcement and cancellation increase as the pair separation decreases. As expected, the symmetry of the equi-displacement contours is influenced by elastic anisotropy, the tetragonality of the point source, and the configuration of the stair-step. Displacements are projected throughout the calculations in order to relate to directional effects that influence diffraction data. It also allows one to assess displacement field anisotropy.

Acknowledgement

The authors acknowledge funding from the National Science Foundation, Grant DMR-8818013, which made this research possible.

References

1. S. M. OHR, *Phys. Stat. Sol.* (*b*) **64** (1974) 317.
2. J. K. LEE, D. M. BARNETT and H. I. AARONSON, *Metall. Trans.* **8A** (1977) 963.
3. D. T. KEATING and A. N. GOLAND, *Acta Metall.* **15** (1967) 1805.
4. H. W. KING, *J. Mater. Sci.* **1** (1966) 79.
5. D. T. KEATING and A. N. GOLAND, *J. Appl. Phys.* **39** (1968) 6018.
6. V. PEROVIC, G. R. PURDY and L. M. BROWN, *Acta Metall.* **27** (1979) 1075.
7. *Idem., ibid.* **29** (1981) 889.
8. J. D. ESHELBY, in "Solid state physics" Vol. 3 (Academic Press, N.Y., 1956) p. 79.
9. S. I. RAO, C. R. HOUSKA, K. S. GRABOWSKI and G. LINKER, *Nuc. Instr. and Meth. in Phys. Res.* **B27** (1987) 396.
10. B. HE, S. I. RAO and C. R. HOUSKA, *J. Mater. Sci.* **25** (1990) 2667.
11. S. I. RAO, E. J. SAVINO and C. R. HOUSKA, in "Mater. Res. Soc. Proc". Vol. 82. Characterization of defects in materials, edited by R. W. Siegel, R. Sinclair, and J. R. Weertman (Materials Research Society, Pittsburgh PA, 1987).
12. A. H. STROUD and D. SECREST, in "Gaussian quadrature formulas (Prentice-Hall, Englewood Cliffs N.J. 1966).
13. C. H. WU, in Ph.D. thesis, Virginia Polytechnic Institute and State University, Blacksburg, VA (1993).
14. B. C. LARSON and F. W. YOUNG, *Phys. Stat. Sol.* **A104** (1987) 273.
15. R. KUZEL, B. HE and C. R. HOUSKA, *J. Mater. Sci.* **32** (1997) 2451.

Received 10 August 1995
and accepted 3 September 1996